Stratospheric aerosols properties from Earth limb photography

M. Ackerman, C. Lippens & C. Muller

Belgian Institute for Space Aeronomy, Circular Avenue, 3, B-1180-Brussels, Belgium

Balloon-borne observation at three wavelengths of visible sunlight scattered by the Earth limb allows the determination of aerosols abundances and size distributions at various altitudes in the stratosphere. The stratospheric aerosols are apparently still under the influence of the Mount St Helens volcanic eruption five months after its occurrence on 18 May 1980.

IT is only relatively recently that detailed studies of the stratospheric aerosols have been initiated. They are of importance because nucleating and catalytic agents are central in determining the radiation balance of the atmosphere. A survey of light scattering techniques used in the remote monitoring of atmospheric aerosols has been published recently[1]. Twilight phenomena have been used both from the ground[2,3] and from satellites, and Earth-limb observation from space has been based on sunlight scattering observed directly[4,5] or through its absorption[6]. *In situ* sampling initiated 20 years ago[7] has also provided much information on the composition of aerosols[8].

We have previously reported[9] the photographic observation, from a balloon gondola floating in the upper stratosphere, of the enhancement of stratospheric aerosols over Europe 23 days after the Mount St Helens volcanic eruption. Several other reports have now appeared[10–13] while details have been provided on the air trajectories which have caused the volcanic plume to move at various altitudes in various directions[14] at the beginning of their many cumbersome revolutions around the Earth. Much information has been collected on the properties of the ejecta in relation to atmospheric effects[15]. On 15 October 1980, five months after the eruption, another photographic balloon flight took place. One of the first observations was finding that the enhancement of stratospheric aerosols below 20 km altitude has become very horizontally homogeneous. This means that it is now possible to determine the basic properties of volcanically influenced aerosols and of natural aerosols which seem to differ in several respects in the stratosphere.

Observation method

Photographic cameras onboard a balloon gondola simultaneously record at various wavelengths the light from the Earth limb below the horizontal line-of-sight while the solar elevation is low. This light is scattered direct sunlight with a contribution from the Earth albedo which is minimized when the Sun is low. The observation geometry is shown in Fig. 1. The limb radiance, R, can be expressed directly in solar radiance units because solar images are recorded simultaneously with a known attenuation factor. The solar elevation is calculated from the time that the picture was taken and from the geographical position. An angular scale is constructed from several consecutive shots. The depression angles at which radiances are measured are related to the line-of-sight altitude of closest approach to the Earth surface taking into account refraction effects[16]. The measured integrated radiances can be inverted taking into account absorption by ozone and air along the line of sight by the 'onion pealing' method to yield the *in situ* radiance, R^*, per unit length versus altitude.

The Sun-oriented gondola can be rotated about its vertical axis so that pictures can be taken at various azimuth angles, A, relative to the Sun's position. The scattering angle θ of direct solar radiation can be computed from the relationship

$$\cos\theta = -\sin D \sin h_\odot + \cos D \cos h_\odot \cos A \qquad (1)$$

where D is the depression angle at which the atmospheric radiance is measured and $h_\odot$ is the solar elevation angle at the time of measurement. As expected from their strong forward scattering properties, aerosols re-emit little light at an azimuth angle 180° away from the direction of the Sun. The limb radiance observed in this case is used to subtract Rayleigh scattering and to isolate aerosols scattering at all azimuths taking into account the Rayleigh phase function[17].

If direct solar radiation only is considered, an *in situ* monodisperse aerosol radiance R_a^* per cm of pathlength is related to the average solar radiance $R_\odot$ by

$$R_a^* = R_\odot \pi \alpha^2 Q_s \sigma \varphi_\theta n / 4\pi \qquad (2)$$

where α is the angular radius of the Sun's disk, 2.16×10^{-5} rad, φ the properly normalized particulate phase function, Q_s the scattering efficiency factor, σ the particulate scattering geometrical cross-section in cm^2 if the number density, n, of the particles is expressed in cm^{-3}.

In practice, our data confirm the previous observation[18] according to which the phase function can, within experimental uncertainties, be represented by the Henyey–Greenstein function. The asymmetry factor g of the phase function and the total scattering efficiency can then be determined. The variation

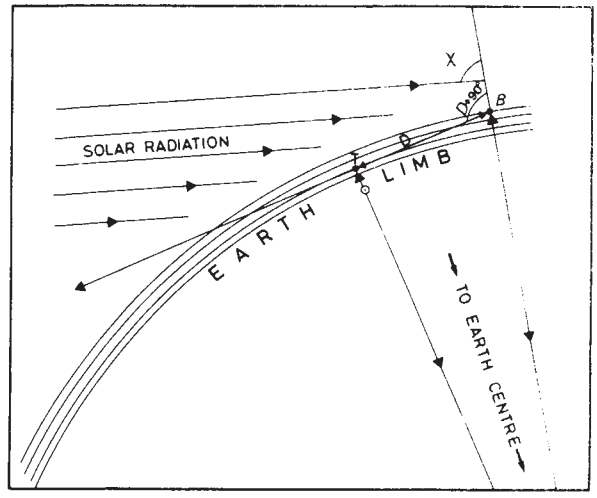

Fig. 1 Observational geometry: quasi parallel light falls on the atmosphere at a solar zenith angle χ, the atmosphere is seen at various depression angles D; through the rotation of the gondola, photographs are taken at various azimuth angles A from the Sun direction.

0028-0836/81/330587—05$01.00

of these parameters with wavelength can be fitted to their theoretical variations using the effective size parameter of Hansen and Travis[19]. This procedure, which uses the Mie scattering computation programme of Wiscombe[20], leads to an evaluation of the effective particle size and provides information on other properties. From these two quantities and from the product $n\sigma$ obtained directly from equation (2) the value of n can be deduced.

The aerosol particle size is usually treated in terms of the wavelength, λ, of the interacting light through the Mie size parameter

$$x = 2\pi a/\lambda \quad (3)$$

where a is the radius of the spherical particle in a monodisperse aerosol. In a polydisperse aerosol the number of particles of radius r is expressed[19] by

$$n_r = Ar^{(1-3b)/b}e^{-r/ab} \quad (4)$$

where a becomes the effective radius while b is a measure of the width of the size distribution; A is a constant related to the total number of particles.

Comparing R_a^* with θ, the scattering angle, at various wavelengths provides information about the asymmetry factor, g. A knowledge of g and its variation with the wavelength of the interacting light leads to the unique determination of a and b. How the scattering efficiency Q_s varies with size parameter can then be determined. The behaviour of these quantities is known from the Mie scattering theory.

Experimental details

The balloon flight took place on 15 October 1980, the tropopause height being 11.4 km. The gondola floated at 37.6 km altitude and was equipped with seven Hasselblad EL 500 cameras with 80-mm focal length lenses and 70-mm films. Four of them were pointing forwards, one being loaded with colour EPR 475 Kodak film, and three in the opposite direction. The six black and white cameras contained (each camera was paired with the one opposite): Wratten filters 47 (440 nm) and 25 (650 nm) with Plus X Kodak film and filters 87 with Kodak aerographic 2424 film (860 nm). To ensure that the Sun images were in the dynamic range of the film, neutral density screens made of exposed and processed sheet films were placed 60 cm from the lenses with their lower edge placed a few centimetres above the optical axis. Before flight, step wedges, inconel filters and samples of the neutral density screens illuminated in parallel light were recorded by each camera in the laboratory. After the flight, the Plus X films were processed using the Kodak D76 developer ($\gamma = 1$) and the IR-sensitive film was processed in the Kodak D19 developer ($\gamma = 2.3$). The dynamic range of this last film was too small to record usefully simultaneous Sun and limb images so that its absolute calibration was derived from the comparison of optical densities due to quasi-pure Rayleigh scattering observed 180° from the Sun in the three colours above 30 km altitude. The absolute calibration in blue and red light was based directly on solar images. The colour, blue, red and IR camera settings (aperture, speed) were respectively: $f/11$, 1/125 s; $f/8$, 1/250 s; $f/8$, 1/250 s; $f/8$, 1/125 s. As soon as the gondola could be Sun oriented, pictures were taken during ascent and later during the float period. With its Sun sensor remaining locked on the Sun, the gondola was then rotated about its vertical axis so that the cameras could record Earth limb images 65°, 115°, 180°, 245° and 295° from the solar azimuth. The whole horizon scan took place between 16.08 and 16.18 h GMT, during which atmospheric illumination conditions changed very little. The latitude and longitude were respectively 1° E and 44° N. The average solar azimuth and elevation angles were 248° and 9.3° respectively. The optical densities were measured on three tracks per frame normally to the horizon by means of a Jarrell–Ash micro-densitometer and subsequently converted into radiance, in units of solar radiance, versus altitude of the grazing line of sight every 200 m. Each photograph allows an horizontal angular coverage of about 34°.

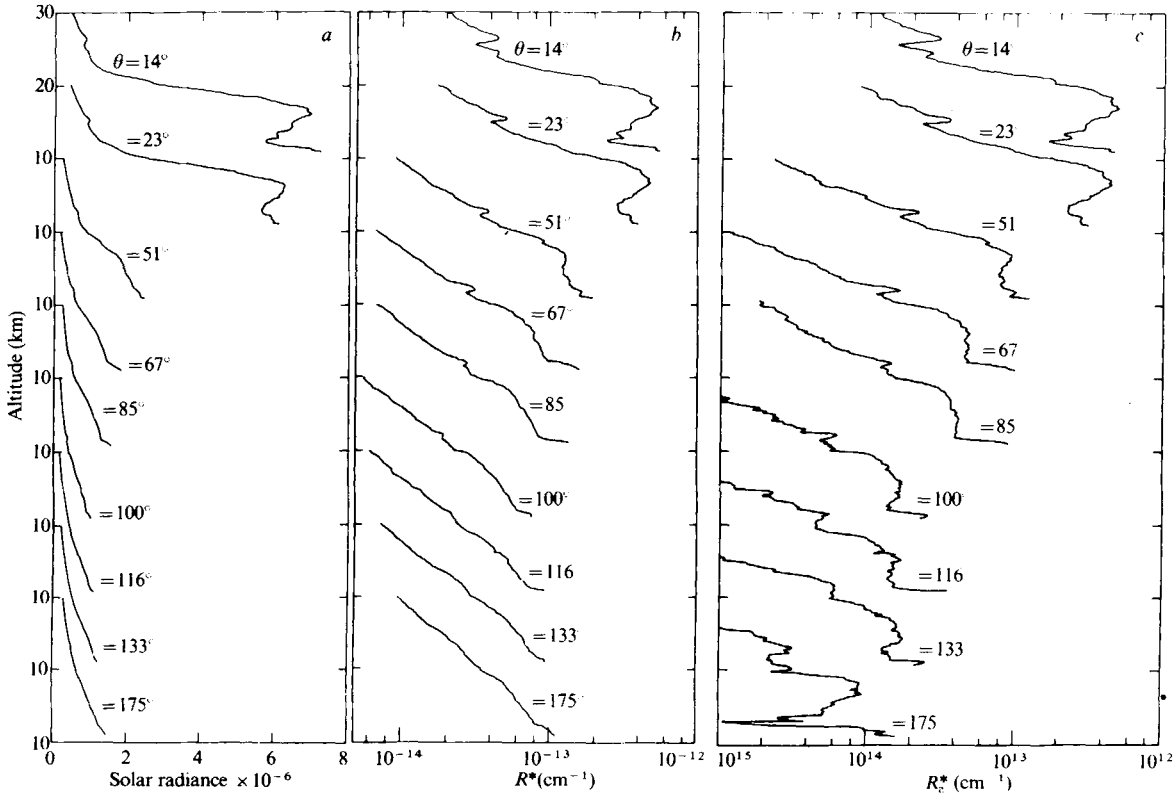

Fig. 2 Data at 650 nm versus altitude for various scattering angles, θ: *a*, integrated radiances, R, along the lines of sight; *b*, inverted radiances, R^*; *c*, inverted radiances due to aerosols, R_a^*. Each successive lower curve is displaced by 10 km altitude from the one above. R^* and R_a^* are expressed in units of solar radiance.

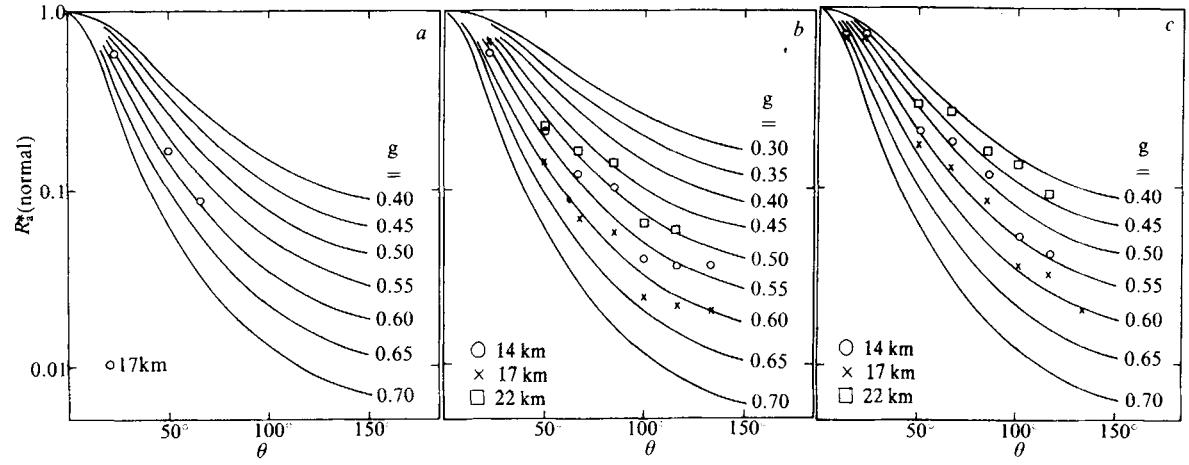

Fig. 3 Henyey–Greenstein phase functions of the radiance versus scattering angles, normalized at $\theta = 0°$ for various values of the asymmetry factor, g. The experimental data points are shown at the three altitudes studied and for the three wavelengths: *a*, 440 nm; *b*, 650 nm; *c*, 860 nm.

Results

As an example, the observed limb radiance values are presented versus the altitude of closest approach of the line of sight to the Earth surface (sea level) for 650 nm and for various scattering angles in Fig. 2*a*.

The comparison of the vertical radiance profiles observed at small scattering angles in red light 11 days before, less than 1 month[9] and five months after the Mount St Helen's eruption shows several characteristics. A radiance enhancement peaking at 17 km altitude still exists on 15 October 1980, by a factor of almost three relative to the pre-eruption value. Above 22 km altitude the radiance has returned to values close to what it was on 7 May 1980. This suggests that the heavy layer observed over England on 6 and 7 June[10] and on 5 June[9] over France constituted the main body of the material injected in the stratosphere by the volcano. Over 5 months, that layer would then have spread in altitude and its centre of gravity would have moved upwards by ~2 km, this being perhaps related to air heating through sunlight absorption by the aerosols.

The various photographs taken around the vertical axis of the gondola reveal the 17 km layer at all azimuth angles; above 20 km altitude a well defined 1-km thick layer is readily seen. Such thin, well separated features have been observed on each of our previous flights and most probably have no relationship with volcanic activity. They belong to the 'natural' stratospheric aerosol. In this particular case the layer is present towards the south from the gondola and absent towards the north. Its altitude is at 22 km from 125° azimuth counted clockwise from the geographical north to ~220° where it begins to rise up to ~25 km at 250° where it splits and becomes invisible. Particulate matter is also present above, what we call here, the 22 km layer. With respect to the horizontal homogeneity, the comparison of the aerosol direct sunlight scattering with the scattering angles is safe for the 17-km layer; for higher altitudes care must be taken.

For the angular study, along the lines-of-sight integrated radiances are inverted using standard ozone and air distributions[21] and their respective absorption cross-sections[17,22]. The *in-situ* radiance values, R^*, in units of solar radiance and per cm along the line-of-sight at the tangent altitude, are presented in Fig. 2*b*. The R^* values at 650 nm (Fig. 2*b*) show at $\theta = 175°$ an exponential dependence versus altitude, as expected, on which some structure and noise is superimposed. At 860 nm in the backward hemisphere where aerosols are expected to bring a small contribution and particularly at 30 km altitude, the variation of R^* with θ fits well the Rayleigh phase function, giving confidence to the very low contribution from the Earth albedo to the observed signal. This is not surprising as the average cloud deck radiance measured at depression angles from 5 to 15° ranges from 7×10^{-7} to 6×10^{-7} of the solar radiance at respective azimuths from 0 to 180° from the Sun. At $\theta = 14°$ and 17 km altitude the aerosol contribution is about 14 times the Rayleigh contribution.

At 650 nm (Fig. 2*b*) the Rayleigh phase function can be fitted to the radiance variation observed in the backward hemisphere at 30 km altitude. In this case, however, the average cloud radiance varies from 6×10^{-6} near the Sun's azimuth to 6×10^{-7} elsewhere. In the forward direction the aerosol contribution to the radiance is 10.8 times the Rayleigh contribution at 17 km. At 440 nm, Rayleigh scattering dominates even if at $\theta = 14°$ it still seems to be five times smaller than aerosol scattering at 17 km. At $\theta = 175°$, R^* grows faster than exponentially at altitudes below 20 km. Multiple scattering here has an important role because the Rayleigh optical thickness on the tangent line of sight reaches unity at 20 km. This occurs at 9 km and at ground level for 650 and 860 nm respectively. In addition the average cloud deck radiance is very high in blue light varying from 1.6×10^{-5} near the Sun to 10^{-6} of the solar radiance elsewhere. The data obtained in blue light can then only be used

Table 1 Summary of balloon-borne results for three characteristic altitudes

Altitude	14 km	17 km	22 km
g_{440}	—	0.6	—
g_{650}	0.55	0.60	0.50
g_{860}	0.52	0.56	0.45
$\sum Q_s n\sigma_{440}$ (cm^{-1})	—	3.2×10^{-8}	—
$(\sum Q_s n\sigma_{440})_{AM}$ (cm^{-1})	—	1.5×10^{-8}	—
$\sum Q_s n\sigma_{650}$ (cm^{-1})	9.4×10^{-9}	1.0×10^{-8}	2.9×10^{-9}
$(\sum Q_s n\sigma_{650})_{AM}$ (cm^{-1})	6.0×10^{-9}	5.8×10^{-9}	1.5×10^{-9}
$\sum Q_s n\sigma_{860}$ (cm^{-1})	1.9×10^{-9}	2.7×10^{-9}	9.3×10^{-10}
$(\sum Q_s n\sigma_{860})_{AM}$ (cm^{-1})	2.4×10^{-9}	3.1×10^{-9}	9.2×10^{-10}
Q_{s440}	—	0.8	—
Q_{s650}	0.14	0.52	0.1
Q_{s860}	0.10	0.35	0.05
$\sum n\sigma_{440}$ (cm^{-1})	—	4×10^{-8}	—
$(\sum n\sigma_{440})_{AM}$ (cm^{-1})	—	1.9×10^{-8}	—
$\sum n\sigma_{650}$ (cm^{-1})	6.7×10^{-8}	1.9×10^{-8}	2.9×10^{-8}
$(\sum n\sigma_{650})_{AM}$ (cm^{-1})	4.3×10^{-8}	1.1×10^{-8}	1.5×10^{-8}
$\sum n\sigma_{860}$ (cm^{-1})	1.9×10^{-8}	7.7×10^{-9}	8.9×10^{-9}
$(\sum n\sigma_{860})_{AM}$ (cm^{-1})	2.4×10^{-8}	8.9×10^{-9}	8.8×10^{-9}
a (μm)	0.042	0.15	0.045
b	3.6	0.6	1.8
V (cm^3)	1.8×10^{-13}	1.5×10^{-13}	7.0×10^{-14}

g, The asymmetry factor of the phase function; $\sum Q_s n\sigma$, the optical aerosol scattering extinction deduced from observed radiances; $(\sum Q_s n\sigma)_{AM}$, the optical aerosol scattering extinction deduced from comparison with the molecular scattering extinction; Q_s, the scattering efficiency factor; $\sum n\sigma$ and $(\sum n\sigma)_{AM}$, the geometric scattering extinctions; a, b, the size distributions parameters; V, the total volume of particles per cm^3 of air at the respective altitudes.

with caution and at small scattering angle. The situation here is different from that in the balloon-borne aureole observation[23] due to the low solar elevation used.

Figure 2c presents the *in situ* radiance due to aerosols R_a^* obtained by subtracting the Rayleigh scattering R_M^*, due to air. R_M^* is evaluated from R^* at $\theta = 175°$ following the 'clean air' procedure currently used in lidar work[24]. R_M^* is then adapted for the various scattering angles considered according to the molecular phase function[17].

Interpretation

The angular dependance of R_a^* has been fitted to the variation of the scattered light intensity with θ computed for various values of the asymmetry factor g of the Henyey–Greenstein function as shown for three wavelengths in Fig. 3. In blue light a few values of θ give useful results. For the reasons discussed above values for the 22-km layer have only been considered for θ between 51° and 116°.

The asymmetry factors so determined are listed in Table 1 with the optical scattering extinction coefficients $Q_s n\sigma$. The values at 440 nm have not been used because a model taking into account the measured cloud radiances indicates a non-negligible contribution of the albedo to the limb radiance. But this contribution is negligible at the larger wavelengths. The observed g values, taking into account that it is probably slightly higher than 0.6 and 440 nm, tend to indicate that a value of the real index of refraction equal to 1.55 (see ref. 25) is observed here. This value will then be used to deduce the size parameter x, and its variation with λ from 650 to 860 nm leads to the values of a and b characterizing the size distribution listed in Table 1. Eventually, the scattering efficiency Q_s can be deduced from a and b following the Mie scattering theory[19].

With the data available, there is, of course, another method of determining $\sum Q_s n\sigma$. From the air σ values[17] and from the air number density n_{air} taken from a model[21] (mid-latitude, spring–autumn) $(n\sigma)_{air}$ can be evaluated. The R_M^* values determined at $\theta = 175°$ by the 'clean air' method[24] are compared with the R_a^* measured and by taking into account the air and aerosols phase

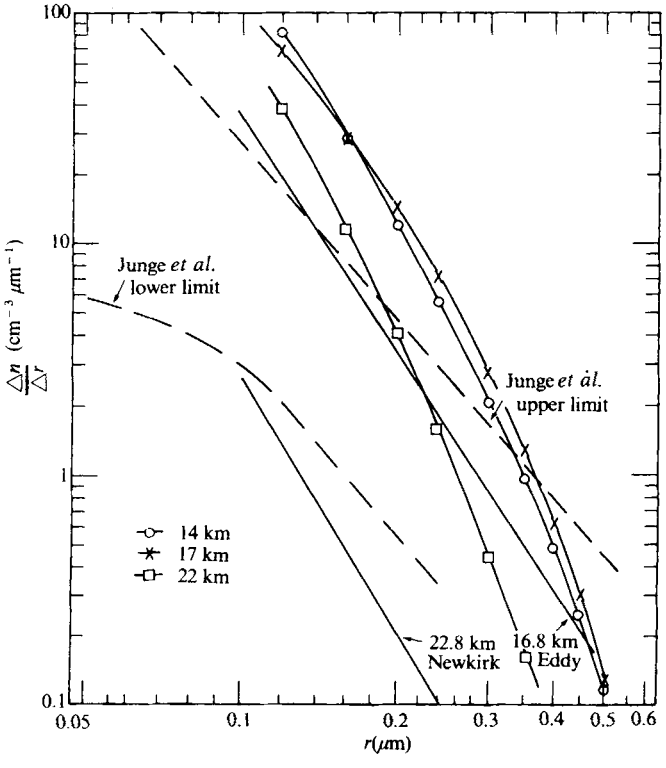

Fig. 4 Number of particles per cm^{-3} versus their radii and per micrometre size interval for three characteristic altitudes: 14, 17 and 22 km. Two previous data sets[7,23] are shown for comparison.

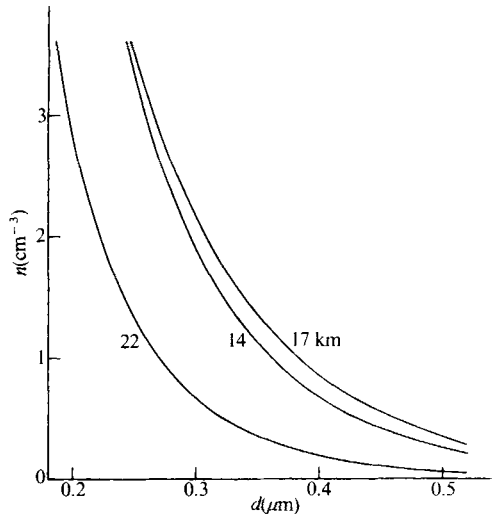

Fig. 5 Total numbers of particles with diameters larger than given values. The ratio of the number of particles with diameters (d) >0.3 μm to the number of particles with diameters >0.5 μm is larger for the layer at 22 km altitude than for 17 and 14 km altitudes indicating the volcanic influence in these two latter cases[29].

functions the values of $(\sum Q_s n\sigma)_{AM}$ for the aerosols are deduced. They are also listed in Table 1.

The absolute particle distribution shown in Fig. 4 for the three altitudes considered is based only on the geometrical extinction coefficient $\sum n\sigma$ at 860 nm for two reasons. In IR light, the albedo contribution to the measurement is negligible while it is a maximum in blue light and in the inversion of R leading to R^* the correction for the absorption by O_3, of which a standard vertical distribution had to be used, is the largest in red light. This is supported by the discrepancy observed at shorter wavelength between the extinctions determined from the observed radiances and those determined by comparison with the molecular scattering. The agreement is very good at 860 nm. The Mie scattering theory also had the best chance to be valid, even if the particles do not exhibit a perfectly spherical and smooth shape, at small values of the size parameter.

Discussion

Our particle distributions are compared in Fig. 4 with the upper and lower limits deduced from *in situ* sampling[7] and with two extreme values resulting from solar aureole measurements[23]. The present results fall within the range of those data except for particles <0.2 μm radius where the upper limit given by Junge *et al.*[7] is exceeded. As mentioned above the aerosols below 20 km are still in volcanically perturbed conditions. On the other hand, the collection efficiency of an *in situ* sampler might be reduced for small particles. Note also that our distributions are steeper especially at large radii. This effect is less pronounced in the comparison with the aureole data. This effect seems to be due to the small values of effective radii obtained here.

Another comparison of our data, shown in Fig. 5, can be made for the total number of particles with a radius >0.15 μm obtained by balloon-borne optical particle counters[26]. The number densities of these particles are 0.4–1.3 particle cm^{-3} in the 14–17 km altitude region and 0.1–0.9 particle cm^{-3} at 22 km. The data presented here for 22 km correspond to a low aerosol content above 20 km and lead to 0.7 particle cm^{-3} above 0.15 μm. At 14 and 17 km altitude the values presented in Fig. 5 respectively imply 1.9 and 2.1 particle cm^{-3} of particles with radii >0.15 μm. A comparison between the two methods would be required to define a possible discrepancy as the aerosols are volcanically enhanced in the present case.

The optical extinction coefficient $Q_s n\sigma$ measured at 1 μm wavelength by the SAM II satellite-borne instrument at low

aerosol load in July 1979[27] exhibits an almost constant value at altitudes from 14 to 20 km of 10^{-9} cm^{-1}. This compares very favourably with our 860 nm value at 22 km. At 17 and 14 km altitude, the extinction in the present case is 3 and 2 times larger. This can be expected from the volcanic influence which may also explain the larger effective particle radius a at 17 km altitude.

A value of the asymmetry factor g of 0.49 ± 0.7 has been measured recently at 633 nm, a wavelength close 650 nm used here, from 10.7 to 12.8 km altitude in the stratosphere[18]. This value corresponds to our measurement at 22 km where the aerosol is considered to be purely 'natural'. Because g is larger in the present case at 14 and particularly at 17 km, one of the volcanic influences must then be to increase the g value and if the Mie theory is applicable to increase the particle size as we observe it at 17 km altitude.

From an optical point of view the particle size distribution, of which the shape is of greater interest than the particle concentration for radiative transfer calculations[25], is variable in the stratosphere. The asymmetry factor, g, is smaller than the constant value (0.7) currently used in models.

For photochemical models of stratospheric aerosols[28] the variable size distribution will have a part to play. The molecular content of the condensed phase thought to be oxidized sulphur, water vapour and perhaps other species is not negligable for the gas phase either as conversion into vapour would lead to volume concentrations in the 10^8–10^9 molecules cm^{-3} at altitudes from 15 to 20 km.

Our measurements therefore confirm recent data and provide new information on critical points which are of fundamental importance in the evaluation of the role that stratospheric aerosols in the size range from 0.04 to 0.4 μm radius can play.

Received 27 April; accepted 25 June 1981.

1. Deirmendjian, D. *Rev. Geophys. Space Phys.* **18,** 341–360 (1980).
2. Bigg, E. K. *Tellus* **16,** 76–83 (1964).
3. Volz, F. E. & Goody, R. M. *J. atmos. Sci.* **19,** 384–406 (1962).
4. Giovane, F., Schuerman, D. W. & Greenberg, J. M. *J. geophys. Res.* **81,** 5383–5388 (1976).
5. Garriott, O. K. *J. opt. Soc. Am.* **69,** 1064–1068 (1979).
6. Rozenberg, G. V. & Nikolaeva-Tereshkova, V. V. *Izv. Atmos. Oceanic Phys.* **1,** 228–232 (1965).
7. Junge, C. E., Chagnon, C. W. & Manson, J. E. *J. Met.* **18,** 81–108 (1961).
8. Cadle, R. D. & Grams, G. W. *Rev. Geophys. Space Phys.* **13,** 475–501 (1975).
9. Ackerman, M., Lippens, C. & Lechevallier, M. *Nature* **287,** 614–615 (1980).
10. Thomas, L., Chaloner, C. P. & Bhattacharyya, S. K. *Nature* **289,** 473 (1981).
11. Reiter, R., Jäger, H., Carnuth, W. & Funk, W. *Geophys. Res. Lett.* **7,** 1099–1101 (1980).
12. D'Altorio, A., Visconti, G. & Fiocco, G. *Geophys. Res. Lett.* **8,** 63–65 (1981).
13. Meixner, F. X., Georgii, H. W., Ockelman, G., Jäger, H. & Reiter, R. *Geophys. Res. Lett.* **8,** 163–166 (1981).
14. Danielsen, E. F. *Science* **211,** 819–821 (1981).
15. Pollack, J. B. *Science* **211,** 815–816 (1981).
16. Link, F. & Neuzil, L. *Tables of Light Trajectories in the Terrestrial Atmosphere* (Hermann, Paris, 1969).
17. Penndorf, R. *J. opt. Soc. Am.* **47,** 176–183 (1957).
18. Grams, G. W. *Geophys. Res. Lett.* **8,** 13–14 (1981).
19. Hansen, J. E. & Travis, L. D. *Space Sci. Rev.* **16,** 527–610 (1974).
20. Wiscombe, W. J. *Appl. Opt.* **19,** 1505–1509 (1980).
21. *U.S. Standard Atmosphere, 1976* (U.S. Government Printing Office, Washington DC, 1976).
22. Ackerman, M. in *Mesospheric Models and Related Experiments* (ed. Fiocco, G.) (Reidel, Dordrecht, 1971).
23. Newkirk, G. Jr & Eddy, J. A. *J. atmos. Sci.* **21,** 35–60 (1964).
24. Grams, G. & Fiocco, G. *J. geophys. Res.* **72,** 3523–3542 (1967).
25. Toon, O. B. & Pollack, J. B. *J. appl. Met.* **15,** 225–246 (1976).
26. Hofmann, D. G., Rosen, J. M., Pepin, T. J. & Pinnick, R. G. *J. atmos. Sci.* **32,** 1446–1456 (1975).
27. McCormick, M. P. *et al. Geophys. Res. Lett.* **8,** 3–4 (1981).
28. Whitten, R. C., Toon, D. B. & Turco, R. P. *Pageophysics* **118,** 86–127 (1980).
29. Hofmann, D. J. & Rosen, J. M. *J. atmos. Sci.* **38,** 168–181 (1981).

Extrachromosomal circular copies of the eukaryotic transposable element *copia* in cultured *Drosophila* cells

Andrew J. Flavell & David Ish-Horowicz

Imperial Cancer Research Fund, Mill Hill Laboratories, Burtonhole Lane, London NW7 1AD, UK

Circular copies of the transposable element copia *have been isolated from cultured* Drosophila *cells. These molecules, which are present at approximately 1 copy per 10–50 cells, comprise a heterogeneous family of related species. Most are composed of a complete copy of the internal section of* copia *combined with either one or two copies of the flanking direct repeat sequences. Such structures are strikingly analogous to the circular proviral forms of retroviruses.*

TRANSPOSABLE genetic elements were first defined genetically in maize[1] and have since been found in a wide variety of organisms including bacteria[2,3], yeast[3] and *Drosophila*[3–5]. They are capable of causing a wide range of genetic effects such as abnormally high mutation and reversion rates and chromosomal deletions or rearrangements. Recent experiments indicate that most, if not all, of these effects are connected with the ability of these elements to transpose to different sites in their host cell genomes. Although there is no direct evidence for analogous species in vertebrates, several observations strongly suggest that eukaryotic transposable elements and the integrated proviral forms of some retroviruses are related.

The following properties are shared by all eukaryotic transposable elements and integrated provirus retroviruses[6–14]:

- Their sequences are each composed of an internal DNA segment several thousand nucleotide pairs long flanked by a pair of identical DNA segments of several hundred base pairs (bp) which are both arranged in the same direct orientation on the element[6–14] (Fig. 1). These repeat sequences are each bounded by small inverted repeats several nucleotide pairs long[7–13].
- The complete element is flanked by an identical pair of host DNA sequences, usually 4–6 bp long, that are present only once in the target site for integration[7,10–12,14].
- There is no detectable homology between the DNA sequences at the insertion site and the ends of the element.
- The terminal dinucleotides of a transposable element or integrated retrovirus provirus are 5′TG . . . CA3′ and in some cases this sequence homology extends further into the elements,

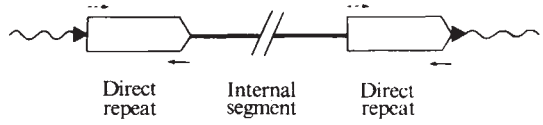

Fig. 1 Generalized structure of a eukaryotic transposable element or integrated retrovirus provirus. An internal segment of several kilobases is bounded by a pair of identical directly repeated sequences. These repeats carry small terminal inverted repeats several base pairs long which are normally imperfect (⇢ and ←). The complete element is flanked by an identical pair of host DNA sequences (►). The flanking genomic DNA is indicated (∿).

0028–0836/81/330591—05$01.00